Solar Energy 188 (2019) 1264–1273

Contents lists available at ScienceDirect

Solar Energy

journal homepage: www.elsevier.com/locate/solener

Modelling and performance evaluation of an integrated receiver-storage for concentrating solar power beam-down system under heterogeneous radiative conditions

Song Yang[a], Jun Wang[a,*], Peter D. Lund[a,b], Chuan Jiang[a], Xiuxiu Li[a]

[a] Key Laboratory of Solar Energy Science and Technology in Jiangsu Province, Southeast University, School of Energy and Environment, No.2 Si Pai Lou, Nanjing 210096, PR China

[b] Aalto University School of Science, P.O. Box 15100, FI-00076 Aalto, Espoo, Finland

ARTICLE INFO

Keywords:
Concentrating solar power
Enhanced heat transfer
Thermal energy storage
Packed bed storage
Beam-down system
Thermocline

ABSTRACT

An integrated receiver-storage (IRS) system for a concentrating solar power (CSP) beam-down system is analyzed for optimal performance and to enable efficient round-the-clock operation. For this purpose, a new in-house programme based on a transient 2-D simulation model coupling a cavity receiver and heat storage together was developed. The programme employs the Matlab® software and it was successfully validated against previous simulation results. The IRS-system was analyzed under realistic radiative boundary conditions. Charging and discharging processes considering radial and axial heat transfer were simulated. It was found that the impact of differences in the heterogeneous radiative boundary conditions on the system efficiencies were limited. The differences between the 2-D coupled model and a decoupled 1-D thermal models were at largest in the start-up of the IRS with a relative error of 5.6%, but the differences smoothened out over time. Analyzing the overall efficiency of the IRS system indicated that the performance of IRS is very good and the IRS could well be applicable for beam-down CSP. Charging and discharging efficiencies of 99% and 93% and a solar-to-exergy conversion ratio of 0.53 could be reached.

1. Introduction

Concentrating solar power (CSP) is a promising renewable energy technology due to its unique features such as dispatchability, which is easily achieved by adding a thermal energy storage unit (TES) to CSP (Kuravi et al., 2013). Recent CSP plants have extensively employed TES (Pelay et al., 2017), which has resulted in increasing efforts to develop efficient and cost-effective TES systems to increase the competitiveness of CSP technologies (Pardo et al., 2014).

There are several approaches to TES for CSP systems based on sensible heat, latent heat, or reversible chemical reactions (Kuravi et al., 2013). Sensible heat storage is the most commonly used TES technology due to its low cost, though the other two have good transient heat transfer characteristics and satisfactory total storage capacity (Pelay et al., 2017; Romero and Steinfeld, 2012). Typical sensible heat storage materials include rock gravel, sand, or concrete (Brosseau et al., 2005; Tamme et al., 2004; Zanganeh et al., 2012). For working fluid, molten salt, steam, or high temperature oil (Gil et al., 2010; Liu et al., 2016; Steinmann and Eck, 2006; Gil et al., 2010; Steinmann and Eck, 2006) are typically employed (Herrmann and Kearney, 2002; Medrano et al., 2010). Air has received less attention than liquid as the heat transfer medium, but combining air with a thermal storage comprised of a packed bed of rocks could have inherent technical and economic advantages (Meier et al., 1991; Zanganeh et al., 2015a; Zanganeh et al., 2012). This paper deals with such a design integrating the CSP receiver and TES into a single integrated unit.

Packed-bed storage is a well-known TES concept and it has been subject to extensive research in the past (Beek, 1962; Geissbühler et al., 2016; Ismail and Stuginsky Jr, 1999; Kunii and Smith, 1960, 1961; Meier et al., 1991; Pfeffer, 1964; Whitaker, 1972; Zanganeh et al., 2014; Zanganeh et al., 2015a; Zanganeh et al., 2015b; Zanganeh et al., 2012). (Kunii and Smith, 1960, 1961) derived the semi-empirical expressions for predicting the effective thermal conductivity of porous rocks with and without stagnant fluid. (Beek, 1962; Pfeffer, 1964) worked on the heat and mass transport for fixed beds corresponding to the Reynolds numbers in different levels. (Whitaker, 1972) proposed the correlations of Nusselt number based on obtained experimental data for heat transfer in packed beds and compact staggered tube bundles.

* Corresponding author.
E-mail address: wj-jw@seu.edu.cn (J. Wang).

https://doi.org/10.1016/j.solener.2019.07.031
Received 6 May 2019; Received in revised form 30 June 2019; Accepted 8 July 2019
Available online 12 July 2019

Nomenclature

Symbols

A_c	area of cross-section (m^2)
c_p	thermal capacity (J/kgK)
d	effective diameter of rocks (m)
F	view factor matrix
G	mass flow rate per unit cross section (kg/m^2s)
H	height (m)
h	enthalpy or heat transfer coefficient (J/kg or W/m^2K)
$\bar{h}$	integrated mean of enthalpy (J/kg)
k	thermal conductivity (W/mK)
L	thickness (m)
$\dot{m}$	mass flow rate (kg/s)
Q	thermal energy (MWh)
$\dot{Q}$	heat flow rate (kW)
q	radiative heat flux (W/m^2)
$\bar{q}$	average radiative heat flux (W/m^2)
R	radius (m)
t	time (s)
T	temperature (K\°C)
ΔT	temperature difference (K\°C)
$\bar{T}$	average cross-section temperature (K\°C)
U	overall heat transfer coefficient (W/m^2K)
X	thermal exergy (MWh)
γ	circulation flow to output flow ratio (-)
δ	Dirac delta function
E	porosity (-)
$\in$	emissivity (-)
η	efficiency (%)
ξ	solar to exergy conversion ratio (-)
ρ	density (kg/m^3)
σ	Stefan-Boltzmann constant or RMSE (W/m^2K^4 or m)
$\|\|$	absolute value

Subscripts

0	initial or original point
absorb	absorbing
bed	packed-beds
c	charging
cav	cavity
comb	combined
conv	convective
cycle	charging-discharging cycle
d	discharging
eff	effective
F	fluid
fan	fan
in	inside
inc	incident
inlet	inlet to the discharging phase
max	maximum
net	net
out	outside
outlet	outlet to the discharging phase
rad-cond	radiative and conductive
ref	reference
s	solid
side	side
sky	sky
surf	cavity surface
top	top
ν	volumetric
W	cavity wall
∞	ambient

Abbreviations

CPC	compound paraboloid concentrator
CSP	concentrated solar power system
GD	Gaussian distribution
HTF	heat transfer fluid
IRS	integrated receiver-storage system
PV	photovoltaic
TES	thermal energy storage
UD	uniform distribution
VF	view factor

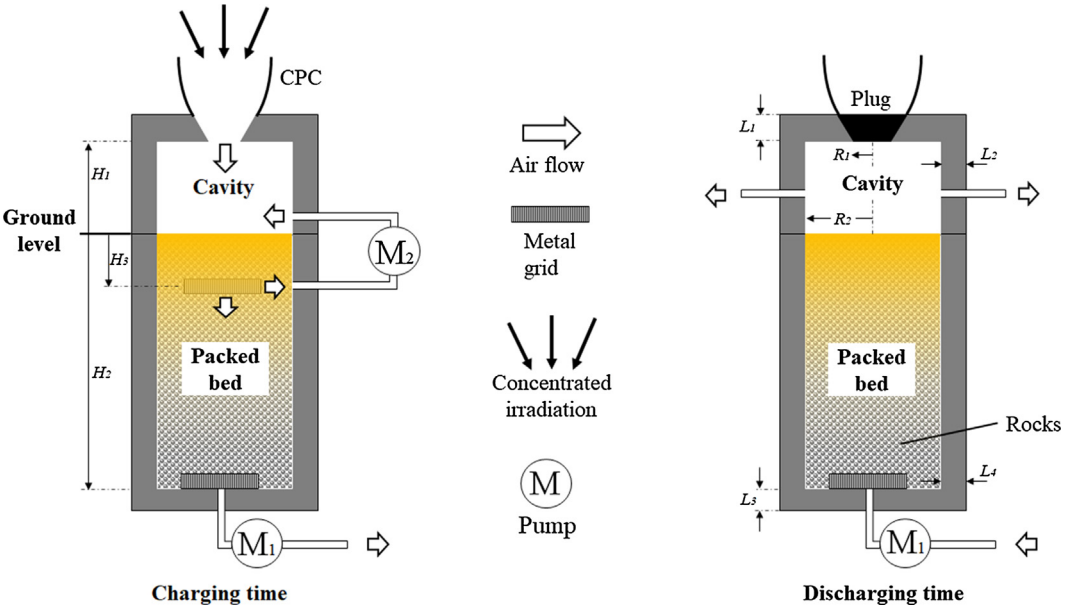

Fig. 1. Scheme of the integrated receiver-storage (IRS) configuration. From (Yang et al., 2019) with permission of the Publisher Elsevier (copyright 2019).

For the beds with the high porosity and complex micro-structure, e.g. reticulate porous ceramic, the radiative transfer equation is necessarily solved and then coupled to the governing equations as the radiative source term (Kaviany, 2012). The computer tomography and the radiative spectroscopy based methodologies have been applied to determine the radiative transport properties of porous media (Ganesan and Lipiński, 2011; Petrasch et al., 2007). In addition, an important theme of research of packed-beds has been the different 1D-3D models for performance analysis of packed beds (Geissbühler et al., 2016; Ismail and Stuginsky Jr, 1999; Meier et al., 1991; Zanganeh et al., 2014; Zanganeh et al., 2015a; Zanganeh et al., 2015b; Zanganeh et al., 2012). Thermocline heat storage for solar tower and dish power systems have also included sensible and phase-change heat transfer issues (Geissbühler et al., 2016; Zanganeh et al., 2014; Zanganeh et al., 2015a; Zanganeh et al., 2015b; Zanganeh et al., 2012). All these have relevance to the modelling effort in this paper, but here we go further in the modelling by considering a new storage design for CSP (integrated receiver-storage).

Previous studies have mainly considered a separate storage unit for CSP, whereas the combined structure of interest in this paper, e.g. the integrated receiver-storage (IRS) has hardly been dealt with in relevant literature. In a previous work, the principle of a novel integrated IRS design has been presented (Yang et al., 2019), which aimed at simplifying the overall structure and finding effective solutions for its use in CSP beam-down plants (Rabl, 1976). This work included simple cavity radiative equilibrium method combined with the 1-D transient air-solid heat transfer to model performance. However, for more precise thermal analysis the effects of heterogeneous radiative boundary conditions and transient cavity radiation processed need to be considered. In this paper, a 2-D transient model was developed filling the research gap and enabling more accurate analysis of the IRS.

The objective of this paper is to present an improved 2-D model for IRS to enable more accurate, sophisticated, and realistic thermal analysis, important to practical designs in CSP applications. The model is applied to cavity and storage analysis, which are the key elements of the IRS. The paper starts by describing the material selection, dimensions, and operating parameters of the IRS-unit chosen for closer analysis here. This is followed in Section 3 by a detailed description of the 2-D modelling approach. Section 4 gives the main results including a comparison to a 1-D model for validation purposes. The paper ends with conclusions in Section 5.

2. Design of the integrated receiver-storage (IRS)

As starting point, an optimal design of IRS reported earlier was chosen here. (Yang et al., 2019). The design is shown in Fig. 1 with main parameters given in Table 1. The system is rated for a 450 kW_{th} beam-down CSP. The operating principle of the IRS is as follows: The top of the packed bed is exposed to concentrated solar irradiation, which heats up the top layer. Cooler air is pumped out from the bottom of the storage with the help of fan M_1, while another fan (M_2) is used to circulate the top air flow for enhancing heat exchange within the bed. The pumping power levels of M_1 and M_2 are subject to the desired output discharging temperature and the scale of the IRS. The charging time is set here to 8 h. During the discharge, air flows through the packed bed inversely and exits from the outlets arranged on the side walls of the cavity. The aperture is closed during discharge preventing hot air from escaping from the top. The discharging time is set to 16 h. Metal grids are used here to eliminate horizontal heterogeneity of flow velocity due to the fan effect.

3. Coupled modelling of heat transfer in cavity and packed-bed storage

To analyze more accurately the thermal performance of the IRS system, a 2-D thermal model is developed here for the IRS taking as starting point a 1-D model for the packed-bed storage (Yang et al., 2019). The main assumptions are as follows:

1) All materials are assumed isotropic and surfaces opaque gray-diffuse;
2) Ambient temperature is 293 K and the sky is a black-body at 8 K lower temperature;
3) Conductive losses through insulation are one-dimensional;
4) Heat losses through the cavity walls during discharging are very small and ignored;
5) Gaussian/uniform distributions are applied as radiative boundary conditions at the cavity bottom;
6) Air is regarded a non-radiative media except for void-to-void radiative heat transfer;
7) Air mass flow rate is uniform at any cross-section perpendicular to the packed bed (plug-flow);
8) Effect of the temperature diffusion to air-phase heat transfer is neglected;
9) Thermal inertia of the walls and the soil insulation layer of storage is not considered.

The model consists of two models both for the cavity and the packed-bed storage, which are combined together. We present the individual models and then their combination in the next.

3.1. Radiation model for cavity inner walls

The radiation modelling of the inner walls of the cavity starts by determining the view factor (VF) for each cavity surface element. For this purpose, the surface is divided into discrete meshes (N_{surf}). After balancing the CPU's time needed and the accuracy of the numerical calculation, the number of nodes in radial, axial, and circumferential directions were set to 30, 20, and 20 respectively. The insulation of the cavity is divided into 35 layers. Finally, Monte Carlo ray tracing with 1 billion photons is employed to calculate the view factor matrix.

Next the radiosity method is used to construct the radiation model for the cavity which determines the relation of the net radiative heat flux (q_{net}) and the temperature at the cavity inside wall ($T_{w,in}$) (Yang et al., 2018):

$$\sum_{j=1}^{N_{surf}} (\delta_{kj} - (1-\in_j)F_{kj})\frac{q_{net,j}}{\in_j} = q_{inc,k} - \sum_{j=1}^{N_{surf}} (\delta_{kj} - F_{kj})\sigma T_{w,in,j}^4 \quad (1)$$

where $q_{inc,j}$ represents the incident radiative heat flux at the j^{th} segment. $\in$ is the emissivity, σ is Stefan-Boltzmann constant (5.6704×10^{-8} W/m^2K^4), δ is the Dirac delta function, and F_{kj} is the VF from the k^{th} to the j^{th} segment.

Table 1
Dimensions and operating conditions of the optimal IRS design.

Dimensions of design		Operating conditions of IRS	
H_1 (m)	1.5	charging time, t_c (h)	8
H_2 (m)	8	discharging time, t_d (h)	16
H_3 (m)	1	HTF's outlet mass flow during charging, $\dot{m}_{1c}$ (kg/s)	0.4
R_1 (m)	0.447	HTF's outlet mass flow during discharging, $\dot{m}_{1d}$ (kg/s)	0.2
R_2 (m)	2	HTF's circulating mass flow during charging, $\dot{m}_{2c}$ (kg/s)	2.4
L_1 (m)	0.7	Circulation flow to output flow ratio, $\gamma = \dot{m}_{2c}/\dot{m}_{1c}$ (-)	6
L_2 (m)	0.7	incident radiation flow rate, $\dot{Q}_{inc}$ (kW)	440
L_3 (m)	1.82	initial temperature, T_0 (K)	298
L_4 (m)	1.82	ambient temperature, T_∞ (K)	293
d (m)	0.003	efficiency of fan, η_{fan} (-)	0.95
ε (-)	0.342	solar-to-power efficiency of commercial CSP, η_{CSP} (-)	0.23

With the special geometric design used here, q_{inc} can just cover the cavity bottom. It is also assumed that it follows a Gaussian distribution (GD) (Eq. (2)) and a uniform distribution (UD) (Eq. (3)) corresponding to the heterogeneous and homogeneous radiative boundary conditions, respectively:

$$q_{inc}(r,\varphi) = \frac{C_0}{2\pi\sigma^2} e^{-\frac{r^2}{2\sigma^2}} \quad (0 \leqslant r \leqslant R_2,\ 0 \leqslant \varphi \leqslant 2\pi) \tag{2}$$

$$q_{inc}(r,\varphi) = \bar{q}_{inc} \quad (0 \leqslant r \leqslant R_2,\ 0 \leqslant \varphi \leqslant 2\pi) \tag{3}$$

where C_0 is a coefficient, $q_0 = \frac{C_0}{2\pi\sigma^2}$ is the peak value of q_{inc} ($r = 0$ m), $\bar{q}_{inc}$represents the average incident radiative heat flux at the cavity bottom set to 3.5×10^4 W/m^2, $\sigma = \frac{R_2}{2}$ and $C_0 = \frac{\pi R_2^2 \bar{q}_{inc}}{1 - e^{-\frac{R_2^2}{2\sigma^2}}}$.

Since q_{net} and $T_{w,in}$ are time-varying and mutually dependent, the transient heat transfer models for the cavity and the storage need to be considered simultaneously.

3.2. 1-D heat transfer model for cavity insulation

The cavity can be separated into two parts: the active area (ACA) and the non-active area (NAA) (Fig. 2). The ACA corresponds to the receiver bottom, i.e. the top surface of the storage, whereas the NAA corresponds to the top and lateral insulations of the cavity. For the NAA, a 1-D transient heat transfer model is adequate given in Eq. (4) accompanied with a convective combined radiative boundary condition for the inner and outer walls in Eqs. (5) and (6):

$$1-D\ heat\ transfer\ model\ for\ the\ NAA: \frac{\partial(\rho_w c_{pw} T_w)}{\partial t} = \begin{bmatrix} \frac{d}{dz}\left(k_w \frac{dT_w}{dz}\right) \\ \frac{1}{r}\frac{d}{dr}\left(r k_w \frac{dT_w}{dr}\right) \end{bmatrix} \tag{4}$$

Boundary conditions:

$$the\ inner\ walls: q_{w,in} = -k_w \begin{bmatrix} \frac{dT_w}{dz} \Big| \begin{matrix} t>0 \\ z = H_1 \end{matrix} \\ \frac{dT_w}{dr} \Big| \begin{matrix} t>0 \\ r = R_2 \end{matrix} \end{bmatrix} = q_{net} - q_{conv} \tag{5}$$

$$the\ outer\ walls: q_{w,out} = -k_w \begin{bmatrix} \frac{dT_w}{dz} \Big| \begin{matrix} t>0 \\ z = H_1 + L_1 \end{matrix} \\ \frac{dT_w}{dr} \Big| \begin{matrix} t>0 \\ r = R_2 + L_2 \end{matrix} \end{bmatrix} = q_{comb} \tag{6}$$

where

$$q_{comb} = \begin{bmatrix} h_{\infty,top} \\ h_{\infty,side} \end{bmatrix} (T_{w,out} - T_\infty) + \epsilon_\infty \sigma (T_{w,out}^4 - T_{sky}^4) \tag{7}$$

$$Initial\ conditions: T_w(t=0) = T_0 \tag{8}$$

q_{net} in Eq. (5) depends on $T_{w,in}$, which varies in time. For the NAA, no energy is utilized and q_{net} thus equals to the sum of the inner convective losses (q_{conv}), the outer combined heat losses (q_{comb}), and the increment of the inner energy inside insulations. For the ACA, T_w is replaced by the temperature of the packed-bed (T_s) which should be coupled with the output of the transient heat transfer model for storage. It will be discussed more in Section 3.3.

The heat transfer coefficients at the top disk ($h_{\infty,top}$) and the lateral wall ($h_{\infty,side}$) of the insulation enclosure in Eq.(7) are modeled using Churchill's and Chen's correlations (Chen et al., 1986; Churchill and Chu, 1975). Note that though q_{conv} is considered as a heat loss in Eq. (5), it can be recovered at the ACA ($q_{absorb} = q_{net} + q_{conv}$) due to the descending air flow which can prevent the convection dissipation through the aperture. Therefore for convenience, q_{conv} is not considered since it has no influence on the results as a whole. Fig. 2 illustrates the different heat transfer mechanisms involved.

Eq. (4) is discretized with the Euler explicit method in time and with the first/second order backward/central difference in space for solving T_w of the NAA, which can be written as Eq. (9) (the top) and Eq. (10) (the side):

$$\rho_w c_{pw,m}^i \frac{T_{w,m}^{i+1} - T_{w,m}^i}{\Delta t} = \frac{k_{w,m}^i (T_{w,m+1}^i - T_{w,m}^i) - k_{w,m-1}^i (T_{w,m}^i - T_{w,m-1}^i)}{\Delta z^2} \tag{9}$$

$$\begin{aligned} &\rho_w c_{pw,n}^i \frac{T_{w,n}^{i+1} - T_{w,n}^i}{\Delta t} \\ &= \frac{k_{w,n-1}^i (T_{w,n}^i - T_{w,n-1}^i)}{r_{n-\frac{1}{2}} \Delta r} \\ &\quad + \frac{k_{w,n}^i (T_{w,n+1}^i - T_{w,n}^i) - k_{w,n-1}^i (T_{w,n}^i - T_{w,n-1}^i)}{\Delta r^2} \end{aligned} \tag{10}$$

3.3. 2-D transient heat transfer model for packed-bed storage

In the 2-D transient heat transfer model for the storage, the air and solid phase are separately modelled in the same 2-D space based on the law of energy conservation shown in Eqs. (11) and (12):

$$\begin{aligned} Solid\ phase: &\frac{\partial((1-\varepsilon)\rho_s c_{ps} T_s)}{\partial t} \\ &= \frac{\partial}{\partial z}\left(k_{eff} \frac{\partial T_s}{\partial z}\right) + \frac{1}{r}\frac{\partial}{\partial r}\left(r k_{eff} \frac{\partial T_s}{\partial r}\right) + h_v (T_f - T_s) \end{aligned} \tag{11}$$

$$Fluid\ phase: \frac{\partial(\varepsilon \rho_f c_{pf} T_f)}{\partial t} + \frac{\partial(c_{pf} G T_f)}{\partial z} = h_v (T_s - T_f) \tag{12}$$

Boundary conditions:

$$\begin{aligned} &T_f \Big| \begin{matrix} t>0 \\ z=0 \end{matrix} = f^{-1}\left[\frac{h_{f,0} + \gamma \tilde{h}_f \Big| \begin{matrix} t>0 \\ z=H_3 \end{matrix}}{1+\gamma} \right]; \qquad \frac{\partial T_f}{\partial z} \Big| \begin{matrix} t>0 \\ z=H_2 \end{matrix} = 0; \\ Charging: &-k_{eff} \frac{\partial T_s}{\partial z} \Big| \begin{matrix} t>0 \\ z=0 \end{matrix} = q_{absorb}; \qquad \frac{\partial T_s}{\partial z} \Big| \begin{matrix} t>0 \\ z=H_2 \end{matrix} = 0; \\ &\frac{\partial T_s}{\partial r} \Big| \begin{matrix} t>0 \\ r=0 \end{matrix} = 0; \qquad -k_{eff} \frac{\partial T_s}{\partial r} \Big| \begin{matrix} t>0 \\ r=R_2 \end{matrix} \\ &\qquad = U_w (T_f - T_\infty). \end{aligned} \tag{13}$$

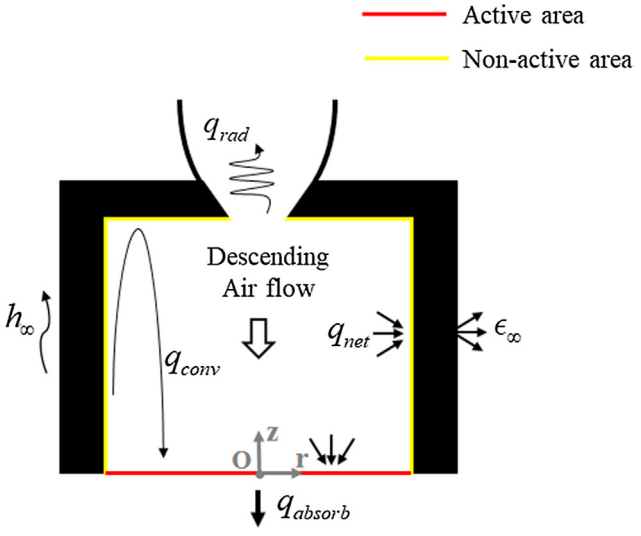

Fig. 2. Illustration of the heat transfer mechanisms in the cavity.

$$T_f \Big|_{z=H_2}^{t>0} = T_0; \qquad \frac{\partial T_f}{\partial z}\Big|_{z=0}^{t>0} = 0;$$

Discharging:

$$\frac{\partial T_s}{\partial z}\Big|_{z=0}^{t>0} = 0; \qquad \frac{\partial T_s}{\partial z}\Big|_{z=H_2}^{t>0} = 0;$$

$$\frac{\partial T_s}{\partial r}\Big|_{r=0}^{t>0} = 0; \qquad -k_{eff}\frac{\partial T_s}{\partial r}\Big|_{r=R_2}^{t>0} = U_w(T_f - T_\infty). \tag{14}$$

Initial conditions: $T_f(t=0) = T_s(t=0) = T_0$. (15)

G represents the mass flow rate per unit cross section equal to $\left(\frac{\dot{m}}{A_c}\right)$. The correlation of Kunii and Smith (Kunii and Smith, 1960; Yagi and Kunii, 1957) is applied here to calculate the effective conductivity of the packed-bed (k_{eff}) which considers the thermal conductivity of both the solid and the fluid as well as the radiative transfer. The volumetric solid-fluid convective heat transfer coefficient (h_v) refers to the model by Alanis et al. and Coutier & Farber (Alanis et al., 1977; Coutier and Farber, 1982). U_w represents the overall wall heat transfer coefficient being used to calculate the heat losses through the walls of the storage (Yang et al., 2019).

Similar to Eqs. (4), (11) and (12) are also discretized with the same methods in time and space for solving T_s and T_f. A grid spacing of 0.066 m in height and 0.067 m in width is used to agree with the cavity meshes as given in Section 3.1. The numerical forms can be written as follows:

$$(1-\varepsilon)\rho_s c^i_{ps,m,n}\frac{T^{i+1}_{s,m,n}-T^i_{s,m,n}}{\Delta t} = \frac{k^i_{eff,m,n}(T^i_{s,m+1,n}-T^i_{s,m,n}) - k^i_{eff,m-1,n}(T^i_{s,m,n}-T^i_{s,m-1,n})}{\Delta z^2} + \frac{k^i_{eff,m,n-1}(T^i_{s,m,n}-T^i_{s,m,n-1})}{r_{n-\frac{1}{2}}\Delta r} + \frac{k^i_{eff,m,n}(T^i_{s,m,n+1}-T^i_{s,m,n}) - k^i_{eff,m,n-1}(T^i_{s,m,n}-T^i_{s,m,n-1})}{\Delta r^2} + h^i_{v,m,n}(T^i_{f,m,n}-T^i_{s,m,n}) \tag{16}$$

$$\varepsilon\rho^i_{f,m,n}c^i_{pf,m,n}\frac{T^{i+1}_{f,m,n}-T^i_{f,m,n}}{\Delta t} + c^i_{pf,m,n}G\frac{T^i_{f,m,n}-T^i_{f,m-1,n}}{\Delta z} = h^i_{v,m,n}(T^i_{s,m,n}-T^i_{f,m,n}) \tag{17}$$

All equations above are mathematically solved using Matlab R2017a®.

3.4. Coupling of the cavity and storage models

The time steps of the two models are set different: 1 s for the cavity and 0.01 s (charging) and 0.02 s (discharging) for the storage, because the change of temperature in a short step (~0.01 s) is too small to impact q_{net}. Therefore, q_{net} for the whole cavity and T_w for the NNA can be regarded constant during a certain number of iterations of the storage model. The time step ratio of 100:1 is fixed as it gives a good accuracy, numerical stability, and reasonable computational speed in the simulations. The flowchart in Fig. 3 illustrates the coupling of the models.

3.5. Validation of the models

A steady radiation model for the cavity receiver (Yang et al., 2018)

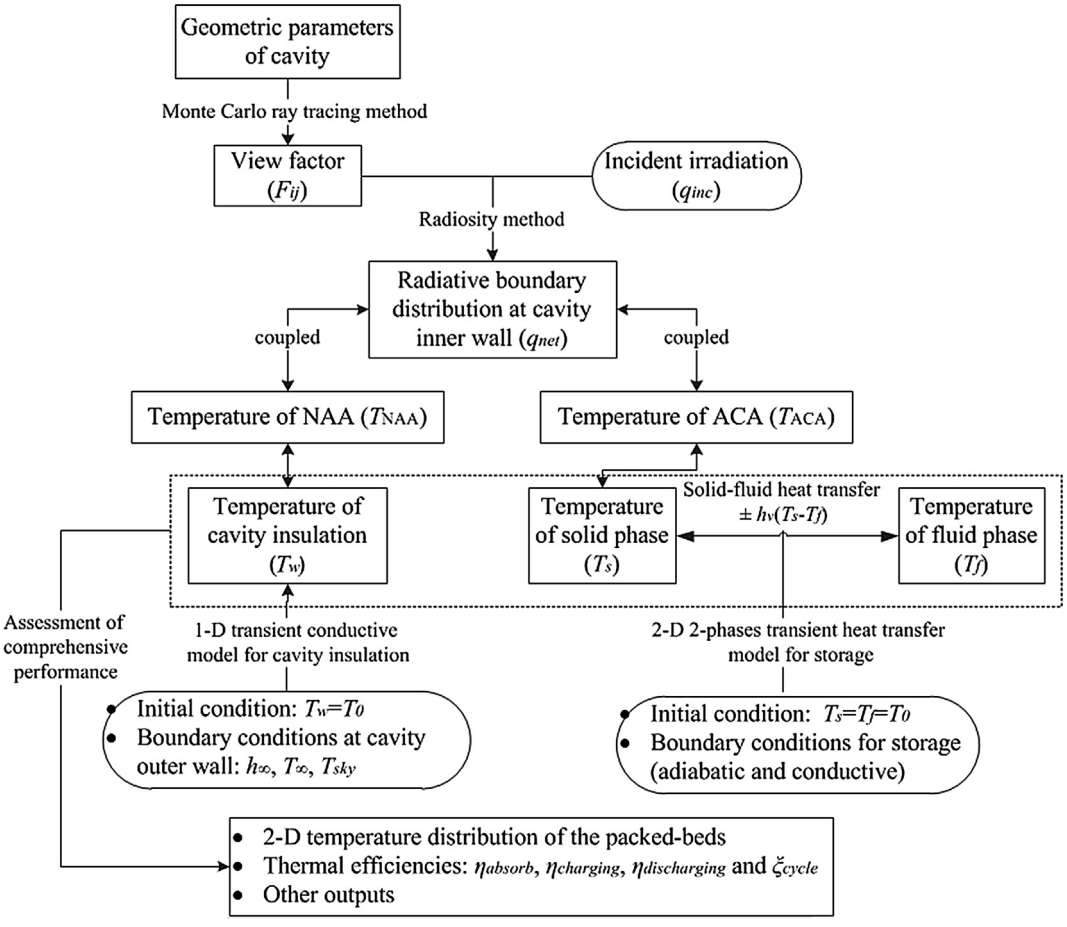

Fig. 3. Flowchart for the coupled heat transfer model of cavity and packed-bed storage.

and a 1-D heat transfer model for the storage (Yang et al., 2019) are used here for validation purposes. Due to the lack of large-scale experimental facilities verification of the model against experimental results was not possible. The models used here for validation have been verified for their accuracy, and simulations results from these are used for our validation exercise. Correspondingly, a cavity heat-pipe receiver for a 2-stage dish concentrator and an IRS for a beam-down system are used for the validation with dimensions and conditions given in the references (Yang et al., 2018; Yang et al., 2019).

3.5.1. Validation of the cavity model

The case of the novel cavity heat-pipe receiver was re-calculated with the new transient radiation-heat-transfer model and compared to previous results. The comparison is between our new model and a steady-state radiation model for the cavity receiver coupled to a 1-D heat transfer model for the storage as stated earlier.

The main difference of the two models is in the transient or steady heat transfer description of the cavity body, meaning that both models should converge in steady-state. Table 2 and Fig. 4 show good agreement between the models for efficiencies, losses and temperature distributions.

3.5.2. 2-D heat transfer model for packed-bed

Next the IRS design was simulated with the new 2-D heat transfer model and the results were compared to our previous numerical results from the 1-D model. The average temperature for each cross-section was calculated from $\bar{T} = f^{-1}(\bar{h})$, where $\bar{h}$ represents the integrated mean of enthalpy which can be determined from Eqs. (18) and (19) below corresponding to the solid and air phases. The reference temperature T_{ref} is set to T_0.

$$\bar{h}_s(T) = \frac{\int_{T_{ref}}^{T}\int_{0}^{R_2} 2\pi r(1-\varepsilon)\rho_s(T)c_{ps}(T)\,dr\,dT}{\int_{0}^{R_2} 2\pi r(1-\varepsilon)\rho_s(T)\,dr} \tag{18}$$

$$\bar{h}_f(T) = \frac{\int_{T_{ref}}^{T}\int_{0}^{R_2} 2\pi r G c_{pf}(T)\,dr\,dT}{\dot{m}} \tag{19}$$

Then $\bar{T}_s$ was compared to T_s from the previous 1-D model under the same conditions. Fig. 5 shows for comparison the temperature profiles in the packed-bed after 5, 15, and 25 cycles. One full cycle represents one charging-discharging cycle over 24 h. The agreement of the results after 5 cycles is very good. The differences found at the start-up phase (< 5 cycles) will be discussed in detail in Section 4.1. In addition, details on the temperature profiles obtained from the 2-D model are also presented in Fig. 6. For each cross-section in Fig. 6, the local temperature varies within a certain range from the maximum point at $r = 0$ m to the minimum point at $r = R_2$. This temperature range which is illustrated as a gray area reduces with the height. It is also observed that the temperature curves from the 1-D model (solid line) fall within the range (0,R_2) given by the 2-D model.

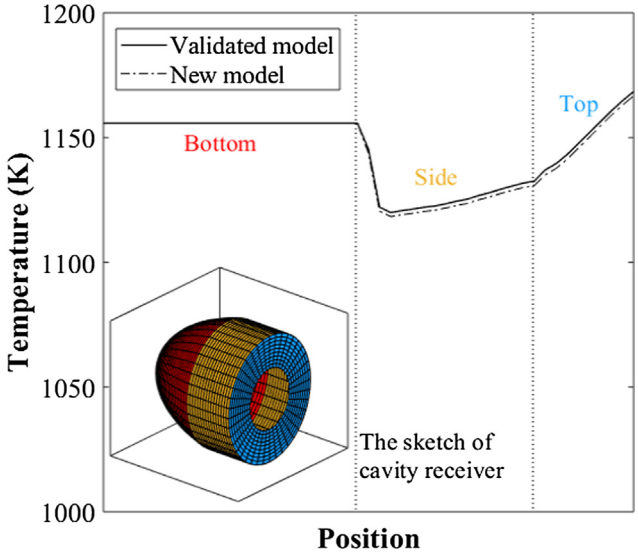

Fig. 4. Temperature distribution at cavity inner walls calculated by the two models.

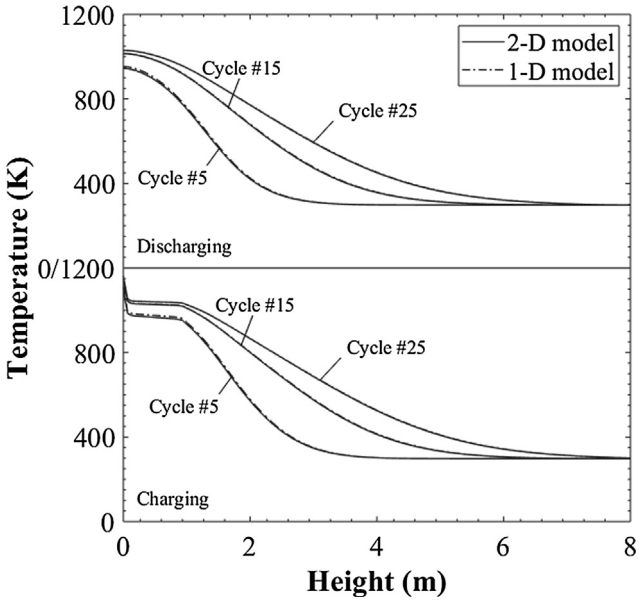

Fig. 5. Simulated IRS performance by the 1-D (solid line) and 2-D (dashed line) models. The temperature curves represent the average temperature for each cross-section ($\bar{T}_s$) vs height at the end of charging (upper) and discharging (lower) cycles #5, 15, and 25.

4. Results and discussion

In the next, a comprehensive performance evaluation of the optimized IRS design is presented. We focus on differences between a 2-D modelling approach with coupled cavity and storage modelling and a 1-D model in which these are decoupled also to identify possible new thermal phenomena in the IRS, the effects of assumptions or approximations used, and also to better understand the applicability range of these design models.

Table 2
Validation of the new transient cavity model.

	Thermal efficiency	Radiative losses	Convective losses	Conductive losses
Validated old steady-state model	90.4%	6.7%	2.3%	0.6%
New transient model	90.3%	6.7%	2.3%	0.7%

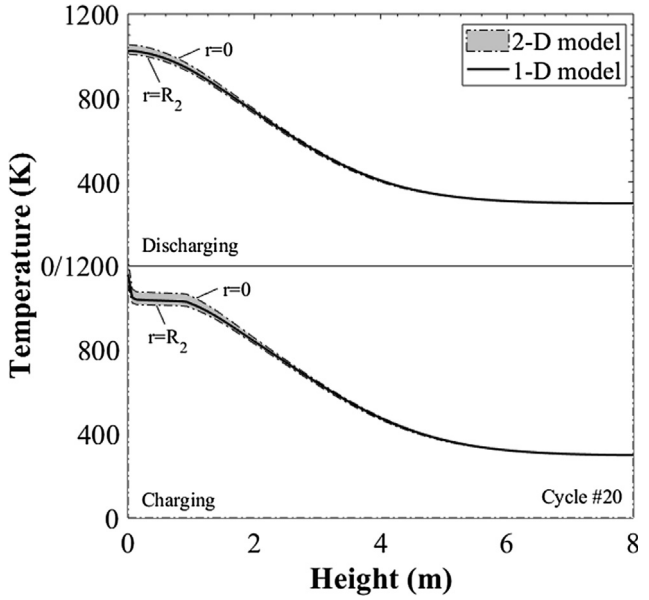

Fig. 6. Temperature curve (1D model) and temperature range (2D model) of packed-beds vs height at the end of charging (upper) and discharging (lower) after 20 cycles. Black solid line: 1D model; Gray area: 2D model.

4.1. Cavity behavior at start-up

During the start-up of the CSP, the thermal inertia of the cavity may play a role for the performance. Typically, in a decoupled model the inertia is neglected, which may lead to overestimating the amount of absorbed solar heat (Q_{absorb}). Whereas in the new 2-D model, the coupling of the cavity and storage is modelled in more detail and should therefore provide more accurate results. In Fig. 7, a comparison of these two modelling approaches for the cavity performance during the start-up is presented. The cavity solar-to-thermal efficiency (η_{cav}) is used as the metrics in the comparison. It is defined as the proportion of heat absorbed (Q_{absorb}) to the incident solar energy (Q_{inc}) during a charge cycle. Eqs. (20)– (22) give the expressions of the relevant functions above.

$$Q_{absorb} = \int_0^{t_c} \left(\int_{ACA} q_{absorb}\, ds \right) dt \tag{20}$$

$$Q_{inc} = \dot{Q}_{inc} \cdot t_c \tag{21}$$

$$\eta_{cav} = \frac{Q_{absorb}}{Q_{inc}} \tag{22}$$

In Eq. (21), $\dot{Q}_{inc}$ represents the concentrated solar heat rate at the cavity bottom as the product of $\bar{q}_{inc}$ and cross-section area (A_c), which is equal to 440 kW in this case. A high η_{cav} is observed in the beginning of the start-up phase (< 5cycles) as the cavity temperature is still relatively low. In the first cycle, the 2-D coupled model gives an efficiency of 88.5%, which is lower than the 93.8% given by the decoupled 1-D model. The reason for the difference is the heat stored inside the cavity insulation which is neglected from the heat losses in the decoupled model. However, the difference diminishes with increasing cycles: after 6 cycles the deviation is rather small ($\Delta\eta_{cav}/\eta_{cav}$ < 1%) and after 25 cycles no difference is observed anymore (η_{cav} = 79.8%).

4.2. 2-D temperature distribution in the packed-bed with different radiative boundary conditions

Another interesting case is the effect of the radiative boundary condition (q_{inc}) at the cavity bottom, i.e. top of the storage, on the temperature distribution in the storage. Two possible distributions, a Gaussian (GD) heterogenous and a uniform (UD) one, were considered here. Fig. 8 depicts 2-D temperature distributions of the vertical section of the beds after 5, 15, and 25 charging cycles using the GD and UD as boundary conditions at z = 0 m. The two temperature gradients are very similar along the z-axis (height), whereas in the radial direction (r) more variations appear. However, if the temperature is averaged along the *r*-axis, a good agreement is observed (see Fig. 5). This in turn indicates that the formation of the vertical thermocline of the storage in the IRS design is less influenced by the distribution of the incident radiative heat flux.

The temperature differences (ΔT) in the *r*-direction can be calculated from the profiles in Fig. 8 as follows:

$$\Delta T(t, z) = T(t, z, r = 0) - T(t, z, r = R_2) \tag{23}$$

Due to the heterogeneity of q_{absorb}, the maximum of ΔT is found at the absorbing surface: at the end of cycle #1 ΔT = 214 K for the GD case and ΔT = −13 K for the UD case, respectively. In the former case, the temperature peak is at r = 0 and drops with increasing r, whereas in the latter case an opposite behavior is found, i.e. the temperature in the central area is slightly lower than the lateral values. Note that q_{absorb} is heterogenous even under a uniform incident radiative condition (UD), because the amount of emission losses through the aperture are larger in the central area than elsewhere. Because of the above mentioned difference, the maximum of $|\Delta T|$ for the GD drops with the number of charging cycles, whereas in the UD case it slightly increases, but in both cases the maximum of $|\Delta T|$ will level out at higher number of cycles (Fig. 9).

4.3. Impact of the heterogeneous radiation

Next the previous analysis is extended to investigate how heterogeneous radiation distributions may affect the overall performance of IRS. In practical applications of CSP, the incident irradiative conditions fall in between the UD and GD cases. Four different indicators are introduced for the analysis covering the different aspects of the IRS performance: cavity heat absorbing efficiency (η_{absorb} or η_{cav}), charging and discharging efficiency ($\eta_{charging}$, $\eta_{discharging}$), and the total solar-to-exergy conversion ratio (ξ_{cycle}). The definitions of these indicators are given in Eqs. (24)–(27):

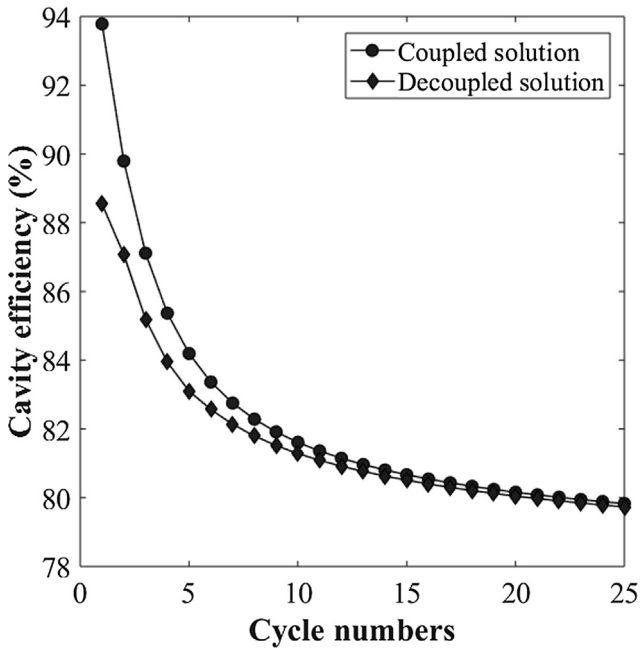

Fig. 7. Comparison of the cavity efficiency (η_{cav}) vs number of cycles calculated by the 1-D decoupled and 2-D coupled model.

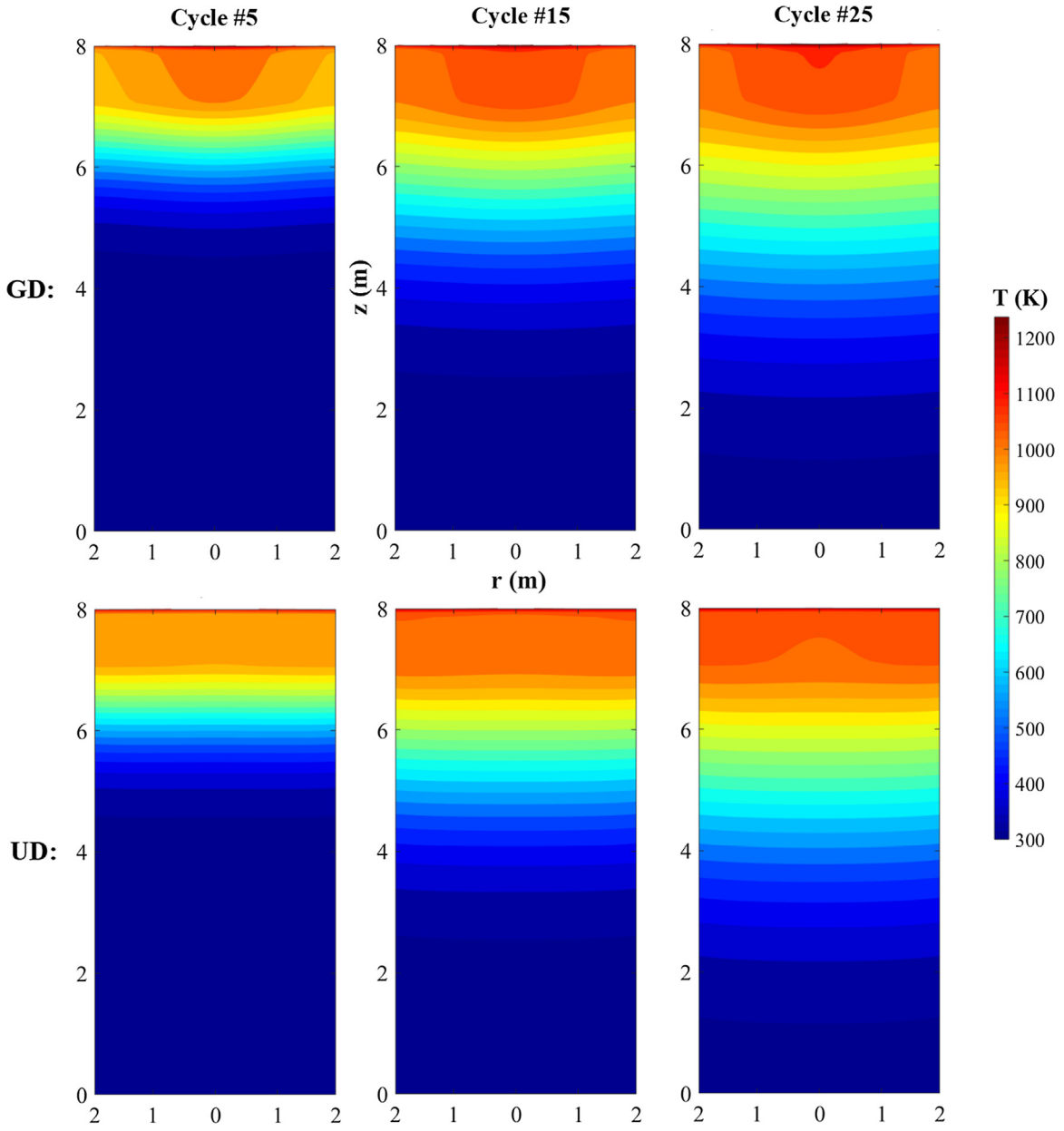

Fig. 8. Isothermal diagrams to the vertical-section of the packed bed after 5, 15, 25 charging cycles using a Gaussian (GD) and uniform distribution (UD) as the boundary condition.

$$\eta_{absorb} = \eta_{cav} = \frac{Q_{absorb}}{Q_{inc}} \tag{24}$$

$$\eta_{charging} = \frac{Q_{charging}}{Q_{absorb}} \tag{25}$$

$$\eta_{discharging} = \frac{Q_{discharging}}{Q_{charging}} \tag{26}$$

$$\xi_{cycle} = \frac{X_{discharging}}{Q_{inc}} \tag{27}$$

where the $Q_{charging}$, $Q_{discharging}$ and $X_{discharging}$ denote the amount of thermal energy and exergy obtained during charging and discharging calculated from the following equations:

$$Q_{charging} = \int_0^{t_c} \left(\int_{V_{bed}} (1-\varepsilon)\rho_s c_{ps} \frac{\partial T_s}{\partial t} dv \right) dt \tag{28}$$

$$Q_{discharging} = \int_0^{t_d} \dot{m}_d (\bar{h}_f(T_{outlet}) - \bar{h}_f(T_{inlet})) dt \tag{29}$$

$$X_{discharging} = \int_0^{t_d} (\dot{m}_d \bar{h}_f(T_{outlet}) - \dot{m}_d \bar{h}_f(T_{inlet})) \left(1 - \frac{T_\infty}{T_{outlet}}\right) dt \tag{30}$$

The differences between the GD and UD cases for these three efficiencies are very small as shown in Fig. 10. Some deviations are observed in η_{absorb}, but less than 0.8% throughout 30 cycles. This minor difference originates from the fact that under the GD condition the central part of the cavity bottom intercepts the most intensive radiation and thus can reach a higher temperature than the lateral part. This may slightly drop down the cavity efficiency, but affects the exergetic conversion ratio (ξ_{cycle}) less than 0.004 units. Therefore, it can be concluded that the impact of the heterogeneous radiative boundary condition is very limited and could be ignored when evaluating the overall performance.

Fig. 10 also shows the dynamic behaviour of the efficiencies over cycles. At the start-up $\eta_{discharging}$ is quite low, but after 10 cycles it

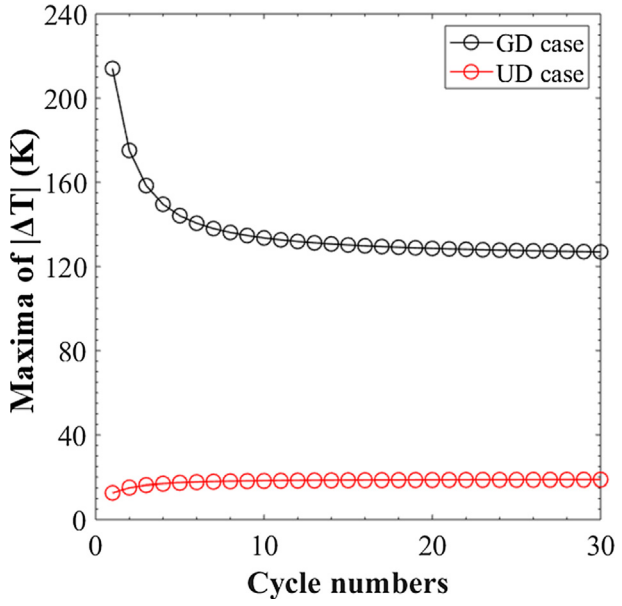

Fig. 9. The maxima of $|\Delta T|$ after each charging cycle.

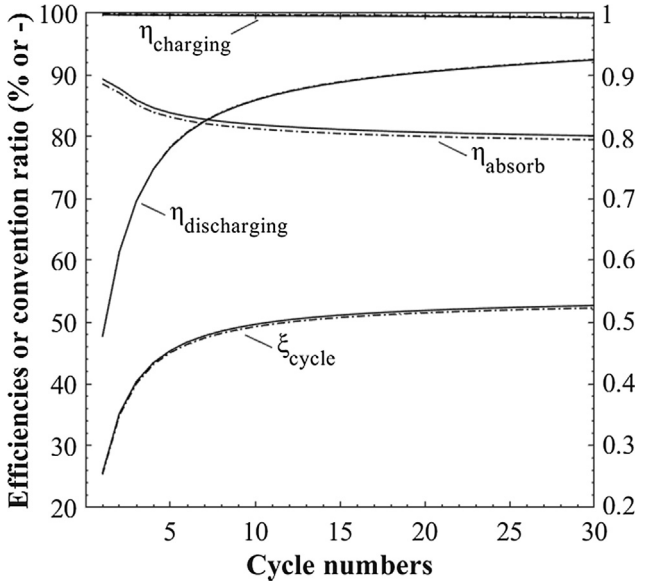

Fig. 10. Behaviour of efficiences (η_{absorb}, $\eta_{charging}$ and $\eta_{discharging}$) and solar-to-exergy conversion ratio (ξ_{cycle}) as a function of number of cycles. UD (solid line), GD (dashed line) cases.

rapidly climbs from 48% to 86%. As a result, ξ_{cycle} improves from 0.26 to 0.50. However, η_{absorb} and $\eta_{charging}$ still drop during this interval, which is mainly because of increasing heat losses through the aperture and the insulation as thermal energy is gradually accumulating and stored in the packed bed. The storage approaches a steady cyclic behaviour after 30 cycles with ξ_{cycle} equal to 0.527. η_{absorb}, $\eta_{charging}$ and $\eta_{discharging}$ have steady state values of 79.5%, 99.2%, and 92.4%, respectively.

4.4. Cavity effect

The maximum temperature differences (ΔT) in the r-direction under the GD condition is 214 K observed at the end of cycle 1, but it reduces to 127 K with higher cycle numbers (Fig. 9). This phenomenon is attributed to the so-called cavity effect in which the impact of heterogenous boundary conditions are effectively offset. Namely, inside the

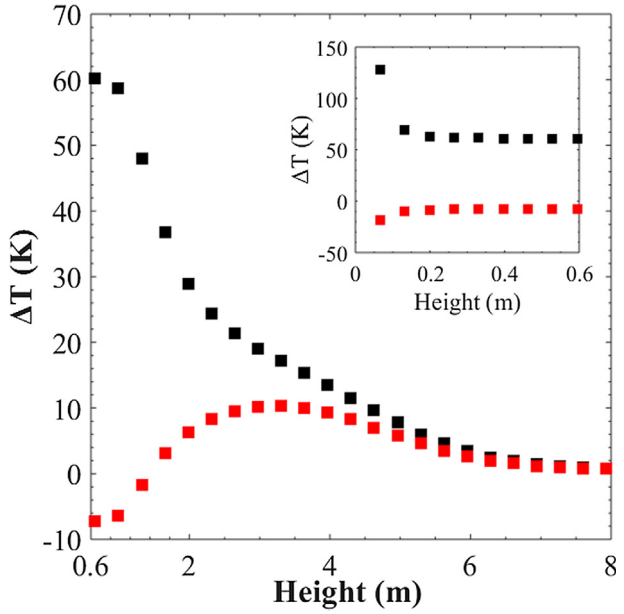

Fig. 11. Radial temperature difference (ΔT) vs height after charge in Cycle 20#. Two radiative boundary conditions at z = 0 m; GD (black square) and UD (red square). (For interpretation of the references to colour in this figure legend, the reader is referred to the web version of this article.)

cavity with a quasi-enclosed structure (Figs. 1 and 2) the interface radiative exchange is enhanced and as a result the temperature distribution at the inner walls tend to be identical when approaching the radiative equilibrium. By contrast, the maximum of $|\Delta T|$ in the UD case is always below 20 K.

However, the ΔT is found to decrease along the z-axis. For example in cycle 20 in the GD case shown in Fig. 11, ΔT quickly drops from the top level down to 0.2 m and then continues to smoothly decrease so that at the storage bottom (z = 8 m) $\Delta T < 1$ K. The reason for such thermal behavior is the negative feedback from the thermal diffusion in r-direction caused by the radial thermal difference that in turn can reduce the difference. Therefore, the heterogeneous boundary condition of the radial temperature distribution can ensure that the ΔT is kept reasonable throughout the bed. Similarly, the UD case in Fig. 11 is also influenced by the feedback effect. ΔT is now negative at the absorbing surface (−19 K in cycle 20). Due to radial diffusion, the temperature difference smoothened at the top of the storage (z < 1.4 m). But contrary to the GD case, ΔT can further increase above zero and reaches peak value of 10 K at z = 3.24 m. This is determined by the conductive heat losses from the lateral insulation, which lead to a lower temperature near the walls. The two temperature curves in Fig. 11 converge to about the same value at the bottom of the storage.

5. Conclusions

In this paper, a detailed 2-D transient thermal simulation model was presented for a novel IRS intended for a beam-down CSP plant. The heat transfer processes in the cavity and the storage were coupled together. The effects of heterogeneous radiation effects on the systematic performance were also analyzed.

The results indicate that the coupled 2-D model well agrees with a simpler decoupled 1-D model proving that the heat transfer modelling of the IRS using a decoupled treatment for the cavity-storage heat exchange is feasible. Also, the differences from the two boundary conditions (Gaussian and uniform distributions) smoothened out soon after the start-up phase indicating that using a uniform radiative boundary condition is justified for long-term performance analyses.

In the start-up phase of operation, the decoupled 1-D model slightly

overestimated the cavity absorbing efficiency (η_{cav}) as the thermal inertia of the cavity insulation was neglected. The maximum η_{cav} in the start-up with the 1-D model simulation was 93.8%, whereas the coupled 2-D model gave 88.5%. This difference disappeared after 5 cycles.

The thermal performance of the storage unit with the two radiative boundary conditions was analyzed in more detail. The averaged radial temperature profiles along the height were similar. Radial temperature differences were observed in both cases: maximum $|\Delta T|$ for the GD case at the top layer was < 214 K and < 20 K for the UD case, respectively. In the GD case, $|\Delta T|$ decreased over time to reach a steady-state value, whereas in the UD case the initial difference was lower and increased to a saturation value, which was explained by cavity effects. Through thermal diffusion $|\Delta T|$ along the height of the bed attenuated over time.

Analyzing the overall efficiency of the IRS system with the 2-D model, indicated that the performance of IRS was very satisfying and would well be applicable for beam-down CSP. Charging and discharging efficiencies of 99.2% and 92.4% and a solar-to-exergy conversion ratio of 0.527 could be reached.

Acknowledgements

This work was supported by the National Science Foundation of China (No. 51736006), the Scientific Research Foundation of Graduate School of Southeast University, China (No. YBPY1855), and Academy of Finland.

References

Alanis, E., Saravia, L., Rovetta, L., 1977. Measurement of rock pile heat transfer coefficients. Sol. Energy 19, 571.
Beek, J., 1962. Design of packed catalytic reactors. Adv. Chem. Eng. 3, 203–271.
Brosseau, D., Kelton, J.W., Ray, D., Edgar, M., Chisman, K., Emms, B., 2005. Testing of thermocline filler materials and molten-salt heat transfer fluids for thermal energy storage systems in parabolic trough power plants. J. Sol. Energy Eng. 127 (1), 109–116.
Chen, T., Armaly, B.F., Ramachandran, N., 1986. Correlations for laminar mixed convection flows on vertical, inclined, and horizontal flat plates. J. Heat Transf. 108 (4), 835–840.
Churchill, S.W., Chu, H.H., 1975. Correlating equations for laminar and turbulent free convection from a horizontal cylinder. Int. J. Heat Mass Transf. 18 (9), 1049–1053.
Coutier, J.P., Farber, E., 1982. Two applications of a numerical approach of heat transfer process within rock beds. Sol. Energy 29 (6), 451–462.
Ganesan, K., Lipiński, W., 2011. Experimental determination of spectral transmittance of porous cerium dioxide in the range 900–1700 nm. J. Heat Transf. 133 (10), 104501.
Geissbühler, L., Kolman, M., Zanganeh, G., Haselbacher, A., Steinfeld, A., 2016. Analysis of industrial-scale high-temperature combined sensible/latent thermal energy storage. Appl. Therm. Eng. 101, 657–668.
Gil, A., Medrano, M., Martorell, I., Lázaro, A., Dolado, P., Zalba, B., Cabeza, L.F., 2010. State of the art on high temperature thermal energy storage for power generation. Part 1—concepts, materials and modellization. Renew. Sustain. Energy Rev. 14 (1), 31–55.
Herrmann, U., Kearney, D.W., 2002. Survey of thermal energy storage for parabolic trough power plants. J. Sol. Energy Eng. 124 (2), 145–152.
Ismail, K., Stuginsky Jr, R., 1999. A parametric study on possible fixed bed models for PCM and sensible heat storage. Appl. Therm. Eng. 19 (7), 757–788.
Kaviany, M., 2012. Principles of heat transfer in porous media. Springer Science & Business Media.
Kunii, D., Smith, J., 1960. Heat transfer characteristics of porous rocks. AIChE J. 6 (1), 71–78.
Kunii, D., Smith, J., 1961. Heat transfer characteristics of porous rocks: II. Thermal conductivities of unconsolidated particles with flowing fluids. AIChE J. 7 (1), 29–34.
Kuravi, S., Trahan, J., Goswami, D.Y., Rahman, M.M., Stefanakos, E.K., 2013. Thermal energy storage technologies and systems for concentrating solar power plants. Prog. Energy Combust. Sci. 39 (4), 285–319.
Liu, M., Tay, N.S., Bell, S., Belusko, M., Jacob, R., Will, G., Saman, W., Bruno, F., 2016. Review on concentrating solar power plants and new developments in high temperature thermal energy storage technologies. Renew. Sustain. Energy Rev. 53, 1411–1432.
Medrano, M., Gil, A., Martorell, I., Potau, X., Cabeza, L.F., 2010. State of the art on high-temperature thermal energy storage for power generation. Part 2—case studies. Renew. Sustain. Energy Rev. 14 (1), 56–72.
Meier, A., Winkler, C., Wuillemin, D., 1991. Experiment for modelling high temperature rock bed storage. Solar Energy Mater. 24 (1–4), 255–264.
Pardo, P., Deydier, A., Anxionnaz-Minvielle, Z., Rougé, S., Cabassud, M., Cognet, P., 2014. A review on high temperature thermochemical heat energy storage. Renew. Sustain. Energy Rev. 32, 591–610.
Pelay, U., Luo, L., Fan, Y., Stitou, D., Rood, M., 2017. Thermal energy storage systems for concentrated solar power plants. Renew. Sustain. Energy Rev. 79, 82–100.
Petrasch, J., Wyss, P., Steinfeld, A., 2007. Tomography-based Monte Carlo determination of radiative properties of reticulate porous ceramics. J. Quant. Spectrosc. Radiat. Transf. 105 (2), 180–197.
Pfeffer, R., 1964. Heat and mass transport in multiparticle systems. Ind. Eng. Chem. Fundam. 3 (4), 380–383.
Rabl, A., 1976. Tower reflector for solar power plant. Sol. Energy 18, 269–271.
Romero, M., Steinfeld, A., 2012. Concentrating solar thermal power and thermochemical fuels. Energy Environ. Sci. 5 (11), 9234–9245.
Steinmann, W.-D., Eck, M., 2006. Buffer storage for direct steam generation. Sol. Energy 80 (10), 1277–1282.
Tamme, R., Laing, D., Steinmann, W.-D., 2004. Advanced thermal energy storage technology for parabolic trough. J. Sol. Energy Eng. 126 (2), 794–800.
Whitaker, S., 1972. Forced convection heat transfer correlations for flow in pipes, past flat plates, single cylinders, single spheres, and for flow in packed beds and tube bundles. AIChE J. 18 (2), 361–371.
Yagi, S., Kunii, D., 1957. Studies on effective thermal conductivities in packed beds. AIChE J. 3 (3), 373–381.
Yang, S., Wang, J., Lund, P.D., Jiang, C., Huang, B., 2018. Design and performance evaluation of a high-temperature cavity receiver for a 2-stage dish concentrator. Sol. Energy 174, 1126–1132.
Yang, S., Wang, J., Lund, P.D., Jiang, C., Li, X., 2019. High performance integrated receiver-storage system for concentrating solar power beam-down system. Sol. Energy 187, 85–94.
Zanganeh, G., Commerford, M., Haselbacher, A., Pedretti, A., Steinfeld, A., 2014. Stabilization of the outflow temperature of a packed-bed thermal energy storage by combining rocks with phase change materials. Appl. Therm. Eng. 70 (1), 316–320.
Zanganeh, G., Khanna, R., Walser, C., Pedretti, A., Haselbacher, A., Steinfeld, A., 2015a. Experimental and numerical investigation of combined sensible–latent heat for thermal energy storage at 575 C and above. Sol. Energy 114, 77–90.
Zanganeh, G., Pedretti, A., Haselbacher, A., Steinfeld, A., 2015b. Design of packed bed thermal energy storage systems for high-temperature industrial process heat. Appl. Energy 137, 812–822.
Zanganeh, G., Pedretti, A., Zavattoni, S., Barbato, M., Steinfeld, A., 2012. Packed-bed thermal storage for concentrated solar power–pilot-scale demonstration and industrial-scale design. Sol. Energy 86 (10), 3084–3098.